

Nonlinear System Identification Nano-drone Benchmark

Riccardo Busetto^{*1}, Elia Cereda^{*1}, Marco Forgione¹, Gabriele Maroni¹, Dario Piga¹, and Daniele Palossi^{1,2}

¹Dalle Molle Institute for Artificial Intelligence (IDSIA), USI-SUPSI, Lugano, Switzerland

name.surname@supsi.ch

²Integrated Systems Laboratory (IIS), ETH Zürich, Switzerland

dpalossi@iis.ee.ethz.ch

Abstract

We introduce a benchmark for system identification based on 75 k real-world samples from the *Crazyflie 2.1 Brushless* nano-quadrotor, a sub-50 g aerial vehicle widely adopted in robotics research. The platform presents a challenging testbed due to its multi-input, multi-output nature, open-loop instability, and nonlinear dynamics under agile maneuvers. The dataset comprises four aggressive trajectories with synchronized *4-dimensional motor inputs* and *13-dimensional output measurements*. To enable fair comparison of identification methods, the benchmark includes a suite of *multi-horizon prediction metrics* for evaluating both one-step and multi-step error propagation. In addition to the data, we provide a detailed description of the platform and experimental setup, as well as baseline models highlighting the challenge of accurate prediction under real-world noise and actuation nonlinearities. All data, scripts, and reference implementations are released as open-source at <https://github.com/idsia-robotics/nanodrone-sysid-benchmark> to facilitate transparent comparison of algorithms and support research on agile, miniaturized aerial robotics.

Keywords: Nonlinear system identification, Benchmarks, Quadrotor

1 Introduction

Standardized benchmarks play a central role in accelerating scientific progress by enabling fair comparison, reproducibility, and rapid testing of new algorithms. Their impact has been particularly evident in machine learning and deep learning, where well-defined datasets and evaluation protocols have catalyzed major breakthroughs [1, 2, 3]. In the field of system identification, the *Nonlinear Benchmark Initiative* [4, 5]¹ serves a similar purpose by promoting reproducible and comparable research efforts, highlighting the importance of high-quality datasets and reference methods for rigorous and comparable evaluation.

However, within the domain of aerial robotics, the availability of such standardized benchmarks remains lim-

ited. While public datasets exist, they typically focus on perception-centric tasks such as visual-inertial odometry or Simultaneous Localization and Mapping (SLAM) [6, 7, 8], rather than dynamical modeling or system identification. Even when high-quality flight data is available from aggressive flight sequences as in [9], it is typically provided as a resource to support a specific method, rather than as a structured benchmark with unified evaluation metrics and diverse baselines. This leaves a gap for researchers who wish to rapidly test and compare new identification algorithms without the burden of designing their own evaluation protocols or reference implementations.

This gap is critical for miniaturized platforms, such as *nano-drones* (quadrotors with a mass below 50 g and a diameter below 10 cm), whose adoption has skyrocketed due to their low cost and suitability for safe indoor operation ([10, 11]). Yet nano-drones operate in a uniquely challenging dynamical regime: their extremely low mass and compact geometry limit the thrust and torque generated by their motors and propellers. Consequently, they are more sensitive to disturbances and less capable of rapid corrective action, making them significantly more challenging to model and control during agile flight compared to standard-sized vehicles. Therefore, this emerging robotic platform represents a compelling candidate for our novel system identification benchmark.

Despite these challenges and the growing scientific interest in such platforms, there is currently no publicly available benchmark that provides real flight data for nano-drones, together with a well-defined evaluation protocol suitable for system identification and control. Existing datasets for small aerial vehicles either offer limited scope, target different tasks, or lack the structure required for systematic algorithmic comparison [12]. As a result, researchers must often collect their own trajectory data, which is typically restricted to simple maneuvers or narrow experimental conditions, thereby preventing reproducibility and slowing progress.

In this work, we introduce a benchmark specifically designed to address this gap. The benchmark is built around the *Crazyflie 2.1 Brushless* nano-quadrotor, a commercially available, open-source hardware and software/firmware platform that has recently gained traction in robotics and control research [13, 14, 10]. Despite its small size, the *Crazyflie* exhibits complex non-linear dynamics, as it is a *multi-input multi-output* system that is inherently *open-loop unstable*,

^{*}Equal contribution.

name.surname@supsi.ch

Corresponding author:

¹available at <https://www.nonlinearbenchmark.org/>

displaying *strongly nonlinear* behavior when operated in aggressive conditions. These characteristics make it an appealing and challenging testbed for nonlinear system identification and model-based control.

The primary contribution of this work is a *ready-to-use, high-quality benchmark* that, to the best of our knowledge, constitutes the first publicly available dataset of real flight trajectories collected on a nano-drone. Importantly, the dataset not only covers favorable or quasi-static motion, but also includes aggressive maneuvers that challenge the dynamics of such a small platform and expose the difficulty of achieving accurate multi-step prediction on highly agile nano-scale vehicles. Specifically, the benchmark provides:

1. **A thoroughly-collected dataset of real flight trajectories** recorded using synchronized onboard sensing and motion-capture ground truth, specifically designed to excite the system across a broad dynamic range. The dataset allows for an *as is* use, without requiring access to costly hardware or motion-capture infrastructure.
2. **A fully specified evaluation protocol** based on multi-step-ahead prediction, enabling consistent and transparent comparison of identification methods.
3. **Reference baseline models**, including a nominal physics model, a hybrid physics–learning architecture, and purely data-driven models, illustrating the intrinsic difficulty of the task and providing starting points for future research.
4. **Open-source data and code**, lowering the barrier to entry for system identification and control studies on agile, miniaturized aerial platforms.
5. **A calibrated motor-speed mapping**, extending the off-the-shelf drone’s firmware with the bidirectional DSHOT protocol for accurate telemetry of the motor speeds (RPM).

The remainder of the paper is organized as follows. Section 2 surveys the relevant literature, identifies the main shortcomings of existing datasets and identification studies, and further motivates the contributions presented in this work. Section 3 provides a detailed description of quadrotor operation, introducing the notation, conventions, and the fundamental dynamic model. Section 4 presents the specific Crazyflie platform and the experimental setup employed for data acquisition. In Section 5, we describe in detail the executed trajectories and the resulting dataset, including preprocessing and the proposed evaluation strategy for this benchmark. Section 6 introduces several baseline models, ranging from a purely physics-based formulation to black-box approaches, for performing N -step-ahead predictions. Finally, Section 7 concludes the paper by highlighting the main challenges and outlining potential directions for future research.

2 Related Work

Research on quadrotor system identification encompasses a wide range of platforms, modeling objectives, and data



Figure 1: Crazyflie 2.1 Brushless nano-drone.

Table 1: Aerial drones taxonomy by vehicle class-size.

Vehicle class	Diameter	Weight	Power	Device
<i>standard-size</i>	≥ 50 cm	≥ 1 kg	≥ 100 W	GPU
<i>micro-size</i>	~ 25 cm	~ 500 g	~ 50 W	CPU
<i>nano-size</i>	~ 10 cm	~ 50 g	~ 5 W	MCU
<i>pico-size</i>	≤ 2 cm	≤ 5 g	≤ 0.1 W	ULP

collection methodologies. In Table 1, we report a taxonomy on aerial vehicles, commonly used in the robotics community. Our taxonomy reports the diameter, weight, total power consumption (both motors and electronics), and onboard processing device of the platforms. The class of devices available onboard is a direct consequence of the total power envelope available, as only $\sim 15\%$ of this total can be spent on the electronics (both sensing and computing), see [15].

Standard-sized drones have a diameter of more than 50 cm, a total power envelope of more than 100 W, and a payload that allows them to afford powerful CPUs and GPUs [16]. Micro-sized drones are slightly smaller in size, but with a lower total power envelope of approximately 50 W, they can still host powerful embedded CPUs, such as NVIDIA Jetson/Xavier devices. Nano-sized drones, with their sub-50 g weight and a few 100s mW for onboard processing, can only afford resource-constrained MicroController Units (MCUs), featuring a few 100s kB on-chip memories. Finally, the smaller class of vehicles is represented by pico-sized UAVs, which are as small as a coin but remain out of reach for widespread adoption [15] and would require Ultra-Low Power (ULP) chips, consuming only a few tens of mW.

In this context, the majority of publicly available datasets have been developed either for standard-sized multirotors or for perception-focused tasks, with only limited attention given to dynamical modeling of nano-scale vehicles. This section reviews the most relevant efforts and highlights the absence of benchmarks tailored to nano-quadrotor system identification.

Aggressiveness of trajectories In the aerial robotics literature, a trajectory is typically considered as *aggressive* when it drives the vehicle through fast translational or rotational motions relative to its actuation capabilities. Concretely, aggressive flight is characterized by (i) translational speeds exceeding 2–3 m/s for nano-scale platforms (and > 10 m/s

for larger multirotors), (ii) angular rates above 400–600°/s, or (iii) linear accelerations approaching or exceeding 1–2 times gravity. Such trajectories induce actuator saturation, strong axis couplings, and aerodynamic effects far from near-hover conditions, all of which are essential for evaluating nonlinear system-identification algorithms.

2.1 System Identification on Larger Quadrotors

Several high-fidelity identification studies target custom or commercial multirotors equipped with specialized sensing. Sun et al. [17] perform gray-box identification of a standard-sized quadrotor using high-speed flight data recorded in the Open Jet Facility wind tunnel, revealing strong aerodynamic interactions at high speed. Bauersfeld et al. [9] propose the NeuroBEM hybrid aerodynamic model for a custom quadrotor, using aggressive free-flight trajectories collected inside a large 25×25×8 m motion-capture arena. While these datasets provide rich aerodynamic information, the platforms are significantly larger than nano-quadrotors and rely on expensive, non-standard infrastructure.

The DronePropA dataset [18] focuses on fault detection in a standard-sized 1.5 kg quadrotor and includes 130 flight sequences with various propeller defects. Although extensive, it targets health monitoring rather than predictive modeling, and the platform size places it far from the dynamical regime of sub-50 g nano-scale vehicles.

2.2 Nano-Quadrotor Identification

Only a limited number of works consider nano-scale platforms. Szécsi et al. [12] study deep-learning-based identification of a Crazyflie 2.1 using simulation data, without releasing real-flight measurements or standardized evaluation protocols. Förster [19] provides an early characterization of the Crazyflie 2.0, identifying inertial parameters, thrust curves, and motor dynamics using separate static and dynamic tests. Their work provides valuable physical insights, but (i) does not include aggressive flight trajectories, (ii) does not release a public dataset, and (iii) does not provide an evaluation protocol for multi-step-ahead prediction. Beyond these studies, several perception-oriented datasets (e.g., VIO/SLAM-focused micro-UAV datasets) include nano-scale platforms. Still, they do not provide the state, actuation, and ground-truth signals required for system identification or control design.

2.3 Positioning of the Contribution

Existing resources suffer from at least one of the following limitations: (i) platforms are medium- or large-scale [17, 9, 18]; (ii) datasets target perception or fault detection rather than dynamical modeling; (iii) data are not publicly available, simulation-only, or not suitable for multi-step prediction; or (iv) no unified evaluation protocol is given.

Table 2 provides a consolidated comparison of existing datasets and system-identification studies on quadrotors, highlighting their limitations in terms of platform size, data availability, aggressiveness of flight trajectories, and suitability as benchmarks. This comparison further motivates

the need for a dedicated nano-drone benchmark, as introduced in this work. Indeed, to the best of our knowledge, no publicly available benchmark provides real, aggressive flight data for a *nano-quadrotor* together with a standardized system-identification protocol and baseline models. The present work fills this gap by releasing a complete benchmark tailored for control and system identification.

3 Quadrotor Model

3.1 Notation

Throughout this paper, scalars are denoted by regular letters s, S , vectors by lowercase bold symbols \mathbf{v} , and matrices by uppercase bold symbols \mathbf{M} . The quadrotor dynamics are formulated using two right-handed reference frames: the inertial *world* frame \mathcal{W} , with axes $\{\mathbf{x}_\mathcal{W}, \mathbf{y}_\mathcal{W}, \mathbf{z}_\mathcal{W}\}$, fixed to the ground and oriented such that $\mathbf{z}_\mathcal{W}$ points upward; and the *body* frame \mathcal{B} , attached to the vehicle, with origin at the center of mass, and equipped with axes $\{\mathbf{x}_\mathcal{B}, \mathbf{y}_\mathcal{B}, \mathbf{z}_\mathcal{B}\}$ oriented as shown in Fig. 2. The orientation of \mathcal{B} with respect to \mathcal{W} is represented by a unit Hamilton quaternion $\mathbf{q} \in \mathbb{H}$ following the scalar-last convention, i.e., $\mathbf{q} = [q_x, q_y, q_z, q_w]^\top$ with $\|\mathbf{q}\| = 1$. The set of all unit quaternions forms the three-dimensional sphere $\mathbb{S}^3 = \{\mathbf{q} \in \mathbb{H} \mid \|\mathbf{q}\| = 1\}$. Each unit quaternion $\mathbf{q} \in \mathbb{S}^3$ is associated with a rotation matrix $\mathbf{R}(\mathbf{q}) \in \text{SO}(3)$ through a smooth mapping $\mathbf{R} : \mathbb{S}^3 \rightarrow \text{SO}(3)$. Finally, the operator \otimes denotes quaternion multiplication.

Unless otherwise specified, vectors are expressed in world coordinates; e.g., \mathbf{p} denotes the position of the drone’s center of mass with respect to \mathcal{W} expressed in world coordinates. To stress that a vector is expressed in a particular reference frame, we attach the frame name as a subscript. For example, $\mathbf{f}_\mathcal{B}$ denotes the forces acting on the drone expressed in the body frame.

3.2 Quadrotor and propeller dynamics

The state $\mathbf{x} \in \mathbb{R}^{13}$ of the quadrotor is defined as:

$$\mathbf{x} = [\mathbf{p}^\top \mathbf{v}^\top \mathbf{q}^\top \boldsymbol{\omega}^\top]^\top, \quad (1)$$

where $\mathbf{p} = [p_x, p_y, p_z]^\top \in \mathbb{R}^3$ [m] is the position of the vehicle’s center of mass expressed in the world frame \mathcal{W} , and $\mathbf{v} = [v_x, v_y, v_z]^\top \in \mathbb{R}^3$ [m/s] is the corresponding linear velocity, also expressed in \mathcal{W} . The unit quaternion $\mathbf{q} = [q_x, q_y, q_z, q_w]^\top$ represents the orientation of the body frame \mathcal{B} with respect to the world frame \mathcal{W} . Finally, $\boldsymbol{\omega} = [\omega_x, \omega_y, \omega_z]^\top \in \mathbb{R}^3$ [rad/s] denotes the angular velocity of the body relative to the world, expressed in body coordinates \mathcal{B} . The components ω_x, ω_y , and ω_z correspond to rotation rates around the body axes $\mathbf{x}_\mathcal{B}, \mathbf{y}_\mathcal{B}$, and $\mathbf{z}_\mathcal{B}$, respectively.

The continuous-time dynamics of the quadrotor can be

Table 2: Comparison of related datasets and system-identification studies on quadrotors.

Work	Class-size	Real/Sim	Application	Open-source	Benchmark	Aggressive
[17]	Micro	Real	Aerodynamics Gray-box SysID	✗	✓	✗
[9]	Standard	Real/Sim	Aerodynamics / Hybrid modeling	✓	✓	✓
[18]	Standard	Real	Fault diagnosis	✓	✗	✗
[12]	Nano	Sim	Learning-based SysID	✗	✓	✗
[19]	Nano	Real	Parameter estimation	✗	✗	✗
This work	Nano	Real	SysID & control	✓	✓	✓

written compactly as:

$$\dot{\mathbf{x}} = \begin{bmatrix} \dot{\mathbf{p}} \\ \dot{\mathbf{v}} \\ \dot{\mathbf{q}} \\ \dot{\boldsymbol{\omega}} \end{bmatrix} = \begin{bmatrix} \mathbf{v} \\ \frac{1}{m} \mathbf{R}(\mathbf{q}) \mathbf{f}_B + \mathbf{g} \\ \frac{1}{2} \mathbf{q} \otimes \begin{bmatrix} \boldsymbol{\omega} \\ 0 \end{bmatrix} \\ \mathbf{J}^{-1}(\boldsymbol{\tau} - \boldsymbol{\omega} \times (\mathbf{J}\boldsymbol{\omega})) \end{bmatrix}, \quad (2)$$

where m is the quadrotor mass, \mathbf{J} is the inertia matrix in body coordinates, $\mathbf{f}_B = [0, 0, T]^\top$ is the total force acting on the drone expressed in the body frame, $\boldsymbol{\tau} = [\tau_x, \tau_y, \tau_z]^\top$ is the control torque vector, and $\mathbf{g} = [0, 0, -g]^\top$ is the gravity vector in world-frame coordinates, with $g = 9.81 \text{ m/s}^2$.

For control design, the input is typically defined as:

$$\mathbf{u}_{ctrl} = [T \ \tau_x \ \tau_y \ \tau_z]^\top, \quad (3)$$

where T is the total thrust acting along the body z_B , and (τ_x, τ_y, τ_z) are the torques about the body axes x_B , y_B , and z_B , corresponding respectively to *roll*, *pitch*, and *yaw* rotations.

In this work, however, we take as input the individual propeller angular velocities (in rad/s):

$$\mathbf{u} = [\Omega_1 \ \Omega_2 \ \Omega_3 \ \Omega_4]^\top, \quad (4)$$

since these are the physical quantities that generate the above-mentioned thrust and torques. Assuming a quadratic relation between the propellers' angular velocities and the resulting forces/torques [20], and considering the “ \times ” quadrotor configuration characterizing the Crazyflie (see Figure 2), the relation between angular velocities (4) and control inputs (3) is given by:

$$\begin{bmatrix} T \\ \tau_x \\ \tau_y \\ \tau_z \end{bmatrix} = \begin{bmatrix} k_F & k_F & k_F & k_F \\ -k_F L & -k_F L & k_F L & k_F L \\ -k_F L & k_F L & k_F L & -k_F L \\ -k_M & k_M & -k_M & k_M \end{bmatrix} \begin{bmatrix} \Omega_1^2 \\ \Omega_2^2 \\ \Omega_3^2 \\ \Omega_4^2 \end{bmatrix}. \quad (5)$$

In (5), k_F and k_M are the thrust and moment coefficients of the propellers, while L is the effective arm length, defined as the orthogonal distance from the nano-drone's center of mass to each rotor projection on the body axes (see Figure 2). The first row expresses the total thrust as the sum of the four rotor contributions, while the remaining rows describe the roll, pitch, and yaw torques resulting from differential thrust and propeller drag.

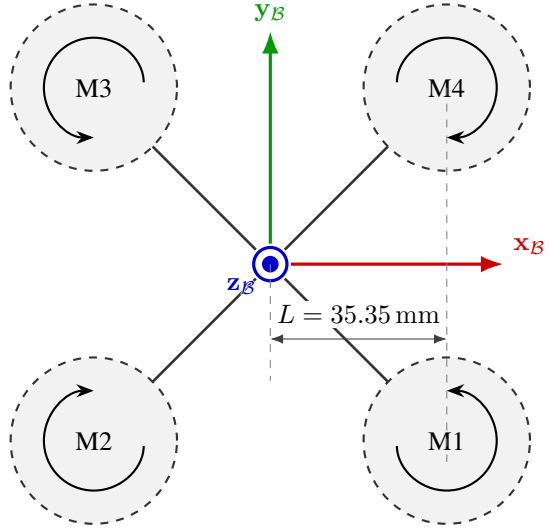


Figure 2: “ \times ” configuration and axis convention adopted in this work (geometry based on [21]).

Remark 1 (Quadratic Rotor Model) Equation (5) relies on the assumption that each propeller produces thrust and torque proportional to the square of its angular speed, with proportionality coefficients k_F and k_M , respectively. Although this approximation suffices to illustrate the main dynamics and remains the standard in quadrotor modeling and control [22], recent advances have produced more accurate descriptions of the aerodynamics [9]. These newer approaches, whether physics-based or data-driven, may offer a more accurate description of drone behavior, particularly during aggressive maneuvers.

4 Experimental Setup

All flights were carried out in the motion-capture arena described below and shown in Figure 3, with safety nets surrounding the test volume in an enclosed room to prevent external air flow during experiments.

4.1 Crazyflie 2.1 Brushless Platform

All experiments were conducted on a Crazyflie 2.1 Brushless nano-quadrotor equipped with a Flow-deck v2 and AI-deck expansion boards. The platform provides on-board computation, sensing, and communication through an STM32F405

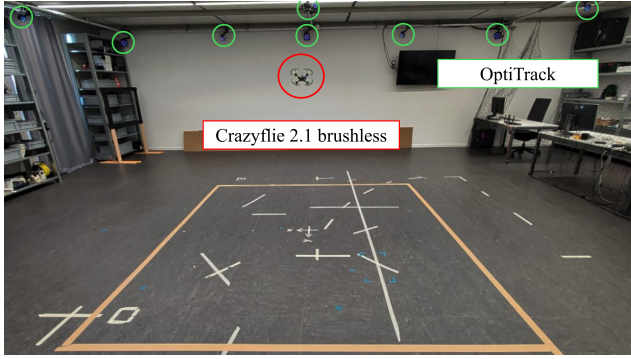


Figure 3: A Crazyflie 2.1 brushless flying in the motion-capture-equipped laboratory.

flight MCU running the official Crazyflie firmware², a Bosch BMI088 6-DOF Inertial Measurement Unit (IMU), and an NRF51822 2.4 GHz low-latency radio. The vehicle is powered by four 8 mm 10000KV brushless motors, driven by EFM8BB21 Electronic Speed Controllers (ESCs) with the Bluejay³ open-source ESC firmware.

The Flow-deck v2 also provides an ST VL53L1X Time-of-Flight laser-based altitude sensor and a PMW3901 optical flow sensor to measure horizontal displacement relative to the ground. The AI-deck provides a Greenwaves Technologies GAP8 System-on-Chip for computation-intensive workloads [14] and an ublox NINA-W102 2.4 GHz WiFi module for high-bandwidth communication. A 1S 350 mA h LiPo battery powers the platform at a nominal voltage of 3.7 V. The total mass of the platform, including the battery, amounts to $m = 45$ g. The inertia matrix $\mathbf{J} = \text{diag}(J_x, J_y, J_z)$ is diagonal due to the symmetric construction. The numerical values of the diagonal entries, taken from the *Crazyflow*⁴ simulator, are: $J_x = 2.3951 \times 10^{-5}$, $J_y = 2.3951 \times 10^{-5}$, $J_z = 3.2347 \times 10^{-5}$ kg \times m².

4.2 Control System

The quadrotor is controlled using a modified version of the geometric controller originally proposed by [23], with integral control action added, as implemented in the Crazyflie's official firmware and running at 500 Hz on the embedded STM32 MCU.

Control setpoints are streamed from a laptop computer over the NRF51 radio using the Crazyswarm⁵ ROS package. The controller tracks a desired position and yaw trajectory $\mathbf{p}_d(t), \psi_d(t)$ by computing the required total thrust T and body torques $\boldsymbol{\tau} = [\tau_x, \tau_y, \tau_z]^\top$ that drive the vehicle toward the reference. The outer position loop computes the desired force vector

$$\mathbf{F}_d = \mathbf{K}_p(\mathbf{p}_d - \mathbf{p}) + \mathbf{K}_i \int (\mathbf{p}_d - \mathbf{p}) dt + \mathbf{K}_d(\dot{\mathbf{p}}_d - \mathbf{v}) + m(\ddot{\mathbf{p}}_d - \mathbf{a})$$

where \mathbf{K}_p , \mathbf{K}_i , and \mathbf{K}_d are proportional, integral, and derivative diagonal matrix gains, while $\ddot{\mathbf{p}}_d$ is the desired feedforward acceleration. The commanded thrust T is then set

²<https://github.com/bitcraze/crazyflie-firmware>

³<https://github.com/bitcraze/bluejay>

⁴<https://github.com/utiasDSL/crazyflow>

⁵<https://imrclab.github.io/crazyswarm2/>

as the component of \mathbf{F}_d along the body's current z -axis: $T = \mathbf{F}_d \cdot z_B$.

The desired orientation \mathbf{R}_d is then constructed with z -axis pointing in the direction of \mathbf{F}_d , while maintaining the reference yaw angle ψ_d . The inner (attitude) loop runs directly on the manifold $\text{SO}(3)$ and computes the angular velocity and torque commands required to track the desired attitude. The attitude error is defined as $\mathbf{e}_R = \frac{1}{2} (\mathbf{R}_d^\top \mathbf{R}(q) - \mathbf{R}^\top(q) \mathbf{R}_d)^\vee$, where $(\cdot)^\vee$ is the standard *vee operator* that unpacks the 3 independent elements of skew-symmetric 3×3 matrices into a vector with 3 components. The angular velocity error is $\mathbf{e}_\omega = \boldsymbol{\omega} - \boldsymbol{\omega}_d$. The control torque is then

$$\boldsymbol{\tau} = -\mathbf{K}_R \mathbf{e}_R - \mathbf{K}_{R,i} \int \mathbf{e}_R dt - \mathbf{K}_\omega \mathbf{e}_\omega,$$

with \mathbf{K}_R , $\mathbf{K}_{R,i}$, and \mathbf{K}_ω the diagonal attitude, integral attitude, and angular-rate gain matrices.

4.3 Sensing and State Estimation

Data were recorded using a combination of onboard sensors and an external motion-capture system. Ground-truth position and orientation were obtained from an *OptiTrack* setup with 18 cameras covering a $6 \times 6 \times 2.5$ m volume.

The onboard sensing suite includes: (i) a 3-axis gyroscope and accelerometer for angular velocity and specific acceleration, (ii) a PMW3901 optical flow module for horizontal velocity estimation, (iii) a VL53L1x time-of-flight sensor for altitude, and (iv) propeller angular velocity measurements obtained from the ESCs via back-EMF zero-crossing detection. These angular velocities values are transmitted to the STM32 flight controller using the bidirectional DSHOT protocol.

State estimation is performed online by an Extended Kalman Filter (EKF) [24, 25], executed at 100 Hz in the Crazyflie firmware. The filter fuses IMU, optical flow, time-of-flight, and motion-capture measurements to provide a full 6-DoF pose estimate, used as feedback by the low-level controller.

Because the official Crazyflie firmware supports only unidirectional DSHOT, we developed a bidirectional driver to enable motor-speed telemetry. The implementation requires precise synchronization of transmit and receive phases across the four motors. We open-source this driver and are integrating it into the official firmware.

5 Dataset and Evaluation Protocol

This section describes the trajectories used to collect the dataset. It provides details on the data itself, as well as the evaluation settings adopted to assess model identification performance on the proposed benchmark. Table 3 summarizes the structure of the recorded dataset, which includes motor speeds $\mathbf{u} = [\Omega_1 \ \Omega_2 \ \Omega_3 \ \Omega_4]^\top$, position and orientation (in quaternion form), angular velocity, and linear acceleration.

5.1 Data Preprocessing

All data is streamed in real-time using high-throughput WiFi streaming through our internally developed NanoCockpit

Table 3: Dataset structure. **Dataset columns** denotes the name of the column in the *csv* file of the provided benchmark dataset.

Variable	Symbol	Unit	Ref. frame	Dataset columns	Measurement source
Timestamp	t	s	–	t	STM32 hardware timer
Inputs					
Propeller speeds	Ω	rad/s	–	$m\{1, 2, 3, 4\}_rads$	Sensorless back-EMF zero crossing
Outputs					
Position	p	m	world	x, y, z	Motion capture + Laser altimeter (z only)
Velocity	v	m/s	world	vx, vy, vz	Optical flow (vx, vy only)
Orientation	q	quaternion	world	qx, qy, qz, qw	Motion capture
Angular velocity	ω	rad/s	body	wx, wy, wz	Gyroscope
Additional					
Specific acceleration	a^{IMU}	m/s ²	body	$a\{x, y, z\}_body$	Accelerometer. It measures $(a - g)_B$

framework and recorded in a `rosbag` file. This recording is asynchronous and timestamped at the source using the onboard STM32 hardware clock. Since the motion-capture system and the flight controller operate at different frequencies and with independent clocks, each experiment required careful post-processing to obtain a time-aligned, uniformly sampled dataset.

Timestamp synchronization Raw data from the Crazyflie firmware and the motion-capture system are first aligned in time by estimating their relative delay. We compute the lag that maximizes the cross-correlation between the position signals (x, y, z) from the OptiTrack and the corresponding onboard estimates, and subtract the average of the three estimated lags to reduce noise sensitivity. After alignment, all channels are resampled to a common 100 Hz rate using interpolation. Because the embedded hardware clock may exhibit irregular sampling intervals, we additionally perform a *retiming* with nearest-neighbor interpolation, to guarantee that all data after processing are uniformly sampled. This also compensates for any potentially missing packets by assigning them the closest available measurement.

Flight-segment extraction Each experiment begins with an initial stationary phase, during which the trajectory is uploaded, and the vehicle takes off. We automatically extract the flight segment by selecting the time interval in which the reference position is non-zero. This produces consistent flight windows across repetitions without manual trimming.

Motor-acceleration alignment Motor speed telemetry is affected by an additional delay in communication and actuation. To compensate for this, we align the motor commands to the inertial measurements by maximizing the cross-correlation between the vertical body acceleration a_z and the instantaneous total thrust, approximated as the sum of squared motor speeds. This yields a robust estimate of the command–actuation delay, ensuring consistent temporal alignment between the thrust input and measured accelerations.

Table 4: Low-pass filter cutoff frequencies for different signal groups ($f_s = 100$ Hz, Butterworth order = 4).

Signal group	Cutoff frequency [Hz]
Position (x, y, z)	10
Linear and angular velocities (v, ω)	18
Linear accelerations (a_x, a_y, a_z)	25
Motor speeds	20
Quaternions (via log-map)	12

Filtering pipeline To reduce measurement noise while preserving dynamic content relevant for system identification, all continuous-valued signals are filtered using zero-phase fourth-order Butterworth low-pass filters. Since different physical quantities exhibit different spectral characteristics, we assign a dedicated cutoff frequency to each signal group. Short gaps in the raw data (up to 10 samples) are filled via bounded interpolation, while longer gaps remain untouched. Quaternion signals are mapped to the rotation-vector representation via the logarithmic map, low-pass filtered component-wise, and mapped back using the exponential map. This procedure ensures that filtering operates in a linear space, avoids quaternion drift or non-unit norms, and preserves the manifold structure of $SO(3)$, which would be violated by direct filtering in quaternion coordinates. Table 4 summarizes the cutoff frequencies applied to each variable group.

5.2 Trajectory Design

Four reference trajectories (named *Square*, *Random*, *Melon*, and *Chirp*) were designed to excite the quadrotor dynamics over a broad range of operating conditions while remaining bounded and repeatable. All trajectories were sampled at 100 Hz and executed at least three times (referred to as *runs*); Square, Random, and Chirp include a 4th run, for a total of 15 flights. The reference paths are illustrated in Figure 4, and their main statistics are summarized in Table 5. Together, these trajectories provide a balanced set of structured, random, and frequency-rich motions for identification and validation.

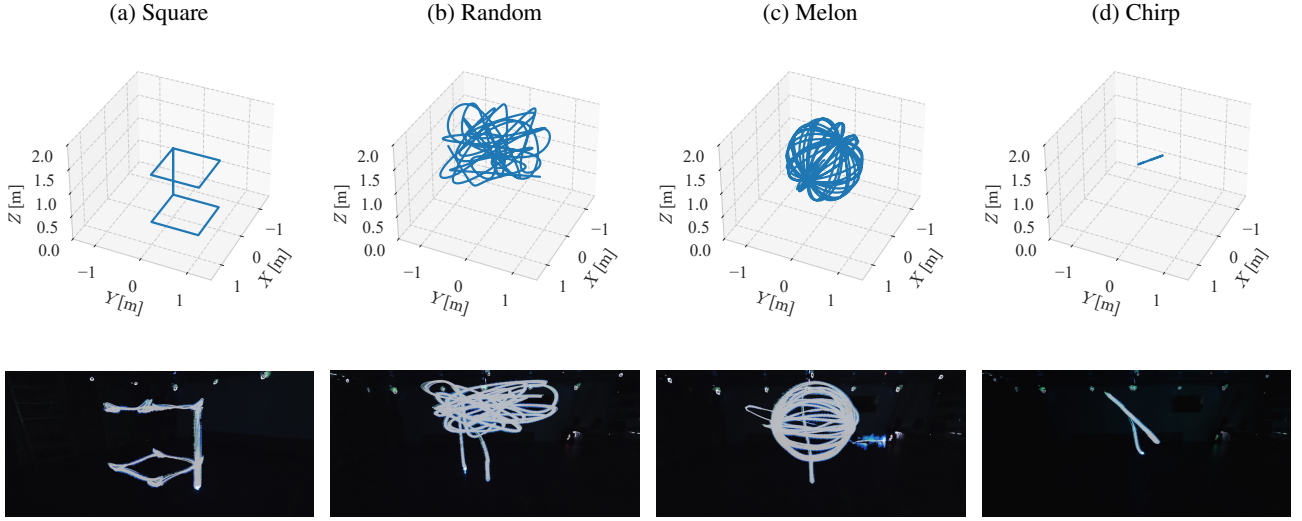


Figure 4: **Reference trajectories and corresponding long-exposure flight traces.** Top row: ideal 3D reference trajectories generated in Python. Bottom row: long-exposure images of Crazyflie 2.1 executing the same trajectories in the motion-capture arena. (Click sub-captions in the PDF viewer to see the animations).

Square A structured path consisting of two horizontal squares of 1 m side length, stacked 1 m apart in height. Each segment is executed in 1 s, followed by 1 s of hovering to allow stabilization between transitions. The motion along each edge is generated using *minimum-snap interpolation*, ensuring continuity in position, velocity, and acceleration. After completing the lower loop, the vehicle ascends to the upper plane, repeats the same pattern, and finally returns to the starting height. This trajectory primarily excites roll and pitch dynamics independently, providing a repeatable planar motion for controller validation.

Random-points A 60 s trajectory composed of 52 waypoints uniformly sampled within a box of size $1 \times 1 \times 0.5$ m centered at $(0, 0, 1.5)$. Positions are interpolated using cubic splines to generate smooth velocity and acceleration profiles. The resulting motion is irregular and non-periodic, with broadband excitation arising from the random spacing of consecutive points.

Melon A smooth, periodic 65 s motion combining elliptical oscillations in the local x - z plane with a slow rotation of the plane about the x -axis $\omega_{\text{plane}} = 0.4$ rad/s. The ellipse radii are fixed to 0.75 m, and the angular velocity to $\omega_{\text{circle}} = 2.5$ rad/s. After the main segment, the drone returns smoothly to the center using a minimum-jerk transition. This trajectory generates coupled translational and rotational motion, providing significant excitation of the attitude dynamics.

Chirp A 60 s trajectory in which the three position axes are simultaneously driven by independent sinusoidal signals of amplitude 0.5 m. The instantaneous frequencies are linearly increased from 0.1 Hz to 0.5 Hz, resulting in a rich spectral content across multiple frequency bands. This trajectory yields persistent excitation of both translational and rotational modes.

Train-test split Experimental data collected from the *Square*, *Random*, and *Chirp* trajectories are used for training, while the *Melon* trajectory is reserved exclusively for testing, yielding 55 999 training samples (74.2%) and 19 497 testing samples (25.8%). We decided to exclude the measured acceleration from the output variables, as it is not a state of the system.

Remark 2 (Zero yaw rate) All trajectories were generated with a fixed yaw orientation, i.e., the reference yaw satisfies $\psi^{\text{ref}} = 0$ throughout the experiments. This choice simplifies the control problem by decoupling yaw from roll and pitch dynamics. It reflects common practice in the identification of drone dynamics, where the focus is typically on modeling translational and attitude dynamics under a constant heading [9].

Table 5: Benchmark statistics for real quadrotor trajectories. Reported values are averaged across runs.

	Duration [s]	v_{mean} [m/s]	v_{max} [m/s]	a_{max} [m/s ²]	Max tilt [°]
Square	19.00	0.83	2.60	12.53	42.95
Random	60.00	1.11	2.69	8.30	43.23
Melon	65.00	1.44	3.06	10.91	56.07
Chirp	60.00	0.88	3.02	10.13	62.69

5.3 Evaluation and Metrics

Let \mathbf{y}_t denote the set of the **Outputs** variables in Table 3 at time t :

$$\mathbf{y}_t = [\mathbf{p}_t^\top \mathbf{v}_t^\top \mathbf{q}_t^\top \boldsymbol{\omega}_t^\top]^\top \in \mathbb{R}^{13}, \quad (6)$$

where $\mathbf{p}_t \in \mathbb{R}^3$ is the position, $\mathbf{v}_t \in \mathbb{R}^3$ the linear velocity, $\mathbf{q}_t \in \mathbb{R}^4$ the unit quaternion representing attitude, and $\boldsymbol{\omega}_t \in \mathbb{R}^3$ the angular velocity. The benchmark evaluates how accurately the model predicts the evolution of the output variables over rolling windows of maximum length $H = 50$ (corresponding to 0.5 s at 100 Hz). At test time, the model receives the true variables \mathbf{y}_t at the beginning of the window and the full input sequence $\{\mathbf{u}_{t+k}\}_{k=0}^{H-1}$, and must predict the future states $\{\hat{\mathbf{y}}_{t+k}\}_{k=1}^H$ without additional state corrections.

Metrics are computed on the held-out *Melon* trajectory $\{(\mathbf{y}_t, \mathbf{u}_t)\}_{t=0}^{T_{\text{test}}-1}$. For each admissible start time $t \in \mathcal{T} := \{0, 1, \dots, T_{\text{test}} - H - 1\}$, the model produces a multi-step open-loop prediction:

$$\hat{\mathbf{y}}_{t+1:t+H} = M(\mathbf{y}_t, \mathbf{u}_{t:t+H-1}).$$

Thus, each start time $t \in \mathcal{T}$ yields a set of H predictions $\{\hat{\mathbf{y}}_{t+1|t}, \dots, \hat{\mathbf{y}}_{t+H|t}\}$, which is compared to the corresponding ground-truth sequence $\mathbf{y}_{t+1:t+H}$ using error metrics defined below.

For positions, linear velocities, and angular velocities, we define the instantaneous Euclidean prediction error at horizon h as:

$$e_{p,t,h} = \|\mathbf{p}_{t+h} - \hat{\mathbf{p}}_{t+h|t}\|_2, \quad (7)$$

$$e_{v,t,h} = \|\mathbf{v}_{t+h} - \hat{\mathbf{v}}_{t+h|t}\|_2, \quad (8)$$

$$e_{\omega,t,h} = \|\boldsymbol{\omega}_{t+h} - \hat{\boldsymbol{\omega}}_{t+h|t}\|_2. \quad (9)$$

For the orientation, we adopt as error metric the geodesic distance on $\text{SO}(3)$ [26] between the true attitude q_{t+h} and its prediction $\hat{q}_{t+h|t}$. The relative rotation is

$$q_{\text{rel},t,h} = q_{t+h}^{-1} \otimes \hat{q}_{t+h|t} = \begin{bmatrix} \mathbf{q}_v \\ q_w \end{bmatrix},$$

with vector part \mathbf{q}_v and scalar part q_w . The corresponding axis-angle rotation error is given by:

$$e_{R,t,h} = 2 \text{ atan2}(\|\mathbf{q}_v\|, q_w), \quad (10)$$

which yields the geodesic orientation error in radians.

We evaluate the prediction accuracy using the mean absolute error per-prediction horizon, defined as:

$$\text{MAE}_{(\cdot),h} = \frac{1}{|\mathcal{T}|} \sum_{t \in \mathcal{T}} e_{(\cdot),t,h}, \quad h = 1, \dots, H, \quad (11)$$

where $(\cdot) \in \{p, v, \omega, R\}$ indicates quantity of interest. For a compact comparison across models, we also report an aggregated simulation error metric, defined as the average prediction error accumulated over a $H = 50$ -step open-loop rollout:

$$\text{MAE}_{(\cdot),1:H} = \sum_{h=1}^H \text{MAE}_{(\cdot),h}. \quad (12)$$

This 50-step simulation error summarizes the model's open-loop performance over a finite horizon, providing a compact indicator of overall simulation quality. For reproducibility, the accompanying repository provides ready-to-use implementations of all the evaluation metrics defined above.

6 Results

All models were implemented in PyTorch with differentiable integration and trained using the data splits described in Section 5.1. Preprocessing, model training, and evaluation were performed on a laptop equipped with an Intel® Core™ i9-14900HX CPU (24 cores, 32 threads), 32 GB of RAM, and an NVIDIA GeForce RTX 4070 Laptop GPU, running Windows 11 (build 22621). The complete implementation is publicly available at <https://github.com/idsia-robotics/nanodrone-sysid-benchmark>.

6.1 Data representation for black-box model learning

As introduced in Section 3, the quadrotor is actuated by four brushless motors whose angular velocities form the input vector $\mathbf{u} \in \mathbb{R}^4$, see (4). Selecting a subset of relevant variables from the measurement vector \mathbf{y} and expressing them in a representation tailored for learning can simplify the regression problem and improve numerical stability.

For example, a direct regression on quaternion orientations $\mathbf{q} = [q_x, q_y, q_z, q_w]^\top$ is undesirable due to the unit-norm constraint and the double-covering property of quaternions, both of which introduce discontinuities in the learning problem. To avoid these issues, we map each quaternion into its equivalent *rotation-vector* (axis-angle) form using the logarithmic map on $\text{SO}(3)$:

$$\mathbf{r} = 2 \text{ atan2}(\|\mathbf{q}_v\|, q_w) \frac{\mathbf{q}_v}{\|\mathbf{q}_v\|}, \quad (13)$$

where $\mathbf{q}_v = [q_x, q_y, q_z]^\top$ is the vector part of the quaternion. The resulting vector $\mathbf{r} \in \mathbb{R}^3$ provides a minimal and topologically consistent parameterization of orientation, free of normalization constraints and sign ambiguities [27].

Using this representation, the output vector used for learning is defined as:

$$\tilde{\mathbf{y}} = [\mathbf{p}^\top \mathbf{v}^\top \mathbf{r}^\top \boldsymbol{\omega}^\top]^\top \in \mathbb{R}^{12}, \quad (14)$$

where $\mathbf{p} = [p_x, p_y, p_z]^\top$ is the position in the world frame \mathcal{W} , \mathbf{r} is the rotation vector obtained from the quaternion orientation, $\mathbf{v} = [v_x, v_y, v_z]^\top$ is the linear velocity in \mathcal{W} , and $\boldsymbol{\omega} = [\omega_x, \omega_y, \omega_z]^\top$ is the body-frame angular velocity.

Training is performed using fixed-length input-output windows of horizon $H = 50$ samples (0.5 s). For each trajectory $j \in \mathcal{J}_{\text{train}} = \{\text{Square}, \text{Random}, \text{Multisine}\}$, with T_j denoting the total number of time samples, the dataset is constructed as:

$$\mathcal{D}_{\text{train}} = \bigcup_{j \in \mathcal{J}_{\text{train}}} \{(\mathbf{X}_t, \mathbf{Y}_t)\}_{t=0}^{T_j-H}, \quad (15)$$

where each pair corresponds to a temporal window:

$$\mathbf{X}_t = \{\tilde{\mathbf{y}}_t, \mathbf{u}_{t:t+H-1}\}, \quad (16)$$

$$\mathbf{Y}_t = \{\tilde{\mathbf{y}}_{t+1:t+H}\}. \quad (17)$$

The same construction is applied to the *Melon* trajectory to obtain the test set $\mathcal{D}_{\text{test}}$.

6.2 Naïve Model

As a reference for evaluating the predictive performance of the proposed models, we consider a constant predictor as a baseline. This model assumes that the system output remains constant over the prediction horizon:

$$\hat{\mathbf{y}}_{t+h|t} = \tilde{\mathbf{y}}_t, \quad h = 1, \dots, H, \quad (18)$$

where $\hat{\mathbf{y}}_{t+h|t}$ denotes the prediction of the output vector $\tilde{\mathbf{y}}_{t+h|t}$ (used for model training) h steps ahead given the current measurement $\tilde{\mathbf{y}}_t$. Although this approach neglects the system dynamics entirely, it establishes a meaningful reference level for short-horizon predictions, since it captures the strong temporal correlation often present in high-rate sampled data. Models that do not outperform this baseline for small horizons h can be considered ineffective, while a consistent improvement indicates that the model has successfully captured meaningful system dynamics.

6.3 Physical model

The nominal physical model is based on the continuous-time quadrotor dynamics given in (2), together with the quadratic aerodynamics equations in (5). The system state is $\mathbf{x} = \mathbf{y} = [\mathbf{p}^\top, \mathbf{v}^\top, \mathbf{q}^\top, \boldsymbol{\omega}^\top]^\top$, while the control input \mathbf{u} corresponds to the four propellers' rotational speeds.

To obtain a discrete-time model suitable for multi-step prediction and simulation, the continuous-time dynamics are numerically integrated over each sampling interval Δt using a fourth-order Runge–Kutta (RK4) scheme. Starting from the current measurement \mathbf{y}_t , the physical model recursively predicts the future outputs as:

$$\hat{\mathbf{y}}_{t|t} = \tilde{\mathbf{y}}_t, \quad (19)$$

$$\hat{\mathbf{y}}_{t+h|t} = f_{\text{phys}}(\hat{\mathbf{y}}_{t+h-1|t}, \mathbf{u}_{t+h-1}), \quad h = 1, \dots, H, \quad (20)$$

where f_{phys} denotes the discrete-time transition function implementing the full rigid-body and motor dynamics. Notice that f_{phys} contains the transformation from axes-angle convention to quaternions and the inverse, to keep consistency with data representation in (16). This model requires the identification of the propeller thrust and drag coefficients, k_F and k_M , which map the normalized motor commands to physical thrust and torque values.

Parameter Estimation The total thrust and torques generated by the propellers are modeled according to the quadratic aerodynamics model in (5), which depends on the unknown coefficients k_F and k_M . To estimate the thrust coefficient k_F , it is convenient to express the translation dynamics (second equation of (2)) in body coordinates: $\mathbf{f}_B = m(\mathbf{a} - \mathbf{g})_B = [0 \ 0 \ T]^\top$. We replace $(\mathbf{a} - \mathbf{g})_B$ with the accelerometer reading \mathbf{a}^{IMU} , which directly measures *specific* acceleration in body frame coordinates: $\mathbf{f}_B \approx \tilde{\mathbf{f}}_B = m\mathbf{a}^{\text{IMU}}$. By considering the force balance along the body's z -axis and by substituting the total thrust T with its constitutive equation from the first row of (5), we get:

$$\tilde{f}_{B,z} = m\mathbf{a}_z^{\text{IMU}} = k_F(\Omega_1^2 + \Omega_2^2 + \Omega_3^2 + \Omega_4^2). \quad (21)$$

The equation above depends on measured quantities and the unknown parameter k_F , allowing for the estimation of the

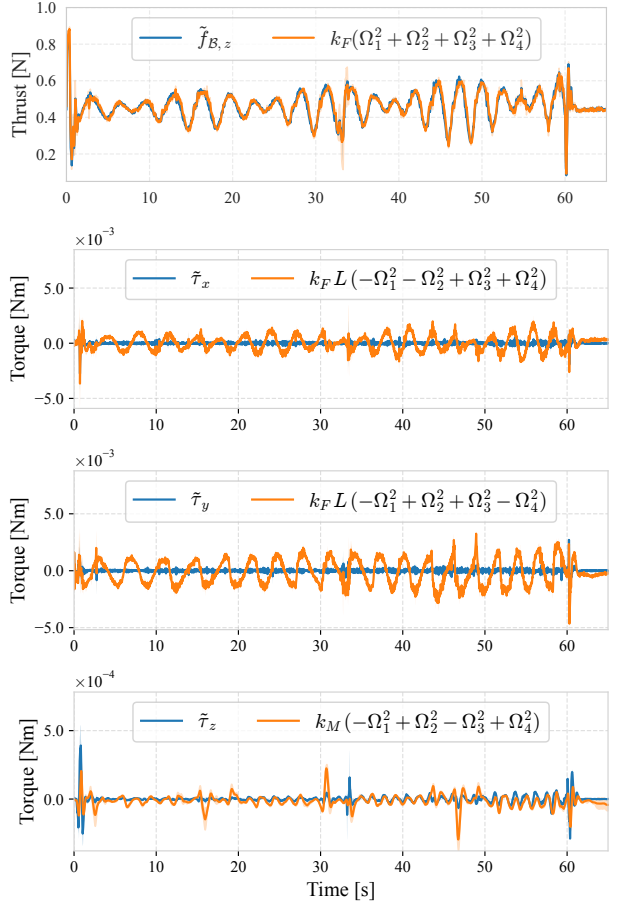


Figure 5: Comparison between measured and model-predicted thrust and yaw torque on the *Melon* test trajectory (run 1), averaged over three runs, using the identified aerodynamic coefficients k_F and k_M .

latter. Least-squares fittings over the training dataset yields $k_F = 3.72 \times 10^{-8} \text{ Ns}^2/\text{rad}^2$.

A similar procedure is used to estimate the torque coefficient k_M . The ground-truth torque signal $\tilde{\tau}$ is first reconstructed as

$$\tilde{\tau} = \mathbf{J}\dot{\boldsymbol{\omega}} + \boldsymbol{\omega} \times (\mathbf{J}\boldsymbol{\omega}),$$

following the rigid body angular dynamics in the last equation of (2). The reconstruction is based on the known inertia matrix \mathbf{J} , the angular velocity $\boldsymbol{\omega}$ measured by the gyroscope, and a finite difference approximation of the angular acceleration $\dot{\boldsymbol{\omega}}$ obtained from the same signal.

Considering the constitutive equation for τ_z at the last row of (5), we get:

$$\tilde{\tau}_z = k_M(-\Omega_1^2 + \Omega_2^2 - \Omega_3^2 + \Omega_4^2). \quad (22)$$

The parameter k_M is then estimated via least-squares regression over the training dataset based on (22). We obtain $k_M = 7.73 \times 10^{-11} \text{ Nms}^2/\text{rad}^2$.

Limitations of the physical model Thrust predictions obtained with the estimated k_F are compared with experimental measurements of the *Melon* trajectory in the top panel of Figure 5. The estimated thrust along z aligns closely with

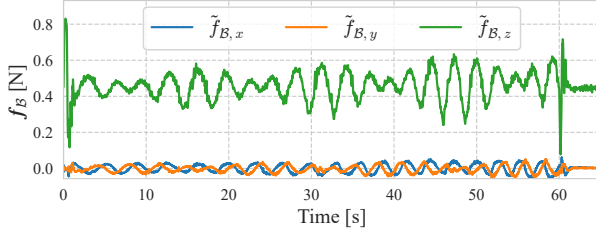


Figure 6: Example of measured forces in body frame. $f_{B,x}$ and $f_{B,y}$ are the non-ideal lateral force components during the *Melon* trajectory (run 1).

the measurements. However, as shown in Figure 6, the reconstructed body frame forces exhibit additional components in the x and y directions that the model does not explain.

The reconstructed yaw torque $k_M(-\Omega_1^2 + \Omega_2^2 - \Omega_3^2 + \Omega_4^2)$ is shown together with the ground truth torque $\tilde{\tau}_z$ in the bottom panel of Figure 5. It appears that the model explains only part of the yaw dynamics.

An even larger model mismatch occurs in the roll and pitch torques, visualized in the second and third panels of Figure 5. For instance, the predicted pitch torque $k_F L(-\Omega_1^2 - \Omega_2^2 + \Omega_3^2 + \Omega_4^2)$ based on the second row of (5) departs significantly from the ground-truth $\tilde{\tau}_x$.

Figure 7 presents a zoomed view of the ground-truth torque roll $\tilde{\tau}_x$, together with its prediction based on the quadratic model. The predicted signal appears to comprise two components: a high-frequency part that agrees with the measured torque and a lower-frequency part that the model cannot account for. This indicates that additional torques, not captured by (5), are acting on the drone.

We hypothesize that the observed lack of fit arises from the limitations of the quadratic model in (5) when applied to aggressive maneuvers, as anticipated in Remark 1. Similar issues have been reported for larger quadrotors [9, 17], although, to our knowledge, they have not yet been investigated at the nano scale.

Since this behaviour is also observed in the training data, in light of the considerations above, we adopt a simplified physical baseline in which $\dot{\omega} = \mathbf{0}$. We stress that this does not imply that the angular acceleration is actually zero. Instead, we retain the portion of the physical model that accurately reflects the underlying dynamics and make a conservative modeling choice for the rotational dynamics, which we later compensate with black box components. Attempts to incorporate the rotational dynamics from the physical equations yielded overall worse results.

6.4 Black-box models

The purely data-driven models learn the state transition directly from data, without explicit physics priors. Both architectures predict the next output as a residual correction on top of the current state. For multi-step prediction, starting from $\hat{\mathbf{y}}_{t|t} = \tilde{\mathbf{y}}_t$, the models are recursively applied as:

$$\hat{\mathbf{y}}_{t+h|t} = \hat{\mathbf{y}}_{t+h-1|t} + f_{bb}(\dots), \quad h = 1, \dots, H, \quad (23)$$

where the structure of f_{bb} depends on the specific architecture described below.

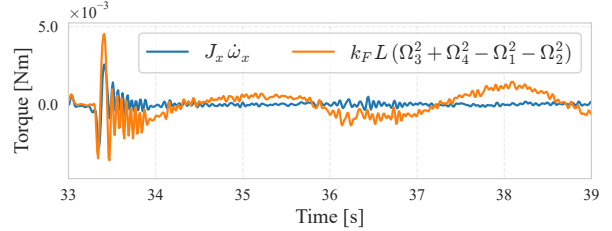


Figure 7: Zoomed comparison between measured and model-predicted thrust and yaw torque on the *Melon* test trajectory (run1).

Rolling Feed-Forward The rolling feed-forward (FF) model implements f_{bb} as a multilayer perceptron (MLP) that outputs the residual increment $\Delta\hat{\mathbf{y}}$ based solely on the immediate state and input. The recursion becomes:

$$\hat{\mathbf{y}}_{t+h|t} = \hat{\mathbf{y}}_{t+h-1|t} + f_{MLP}(\hat{\mathbf{y}}_{t+h-1|t}, \mathbf{u}_{t+h-1}). \quad (24)$$

It captures instantaneous nonlinear relationships between state and input, providing a purely static approximation of the residual dynamics.

Long Short-Term Memory The LSTM model extends the residual formulation by introducing a recurrent hidden state \mathbf{h} , which evolves dynamically over the prediction horizon. To properly initialize the internal dynamics from the static observation \mathbf{y}_t , the initial hidden state is inferred via a dedicated mapping $\mathbf{h}_{t|t} = f_{init}(\tilde{\mathbf{y}}_t)$, parameterized as a small MLP. The multi-step prediction is then generated via the coupled update law:

$$\mathbf{h}_{t+h|t} = \phi_{LSTM}(\mathbf{h}_{t+h-1|t}, \hat{\mathbf{y}}_{t+h-1|t}, \mathbf{u}_{t+h-1}), \quad (25a)$$

$$\hat{\mathbf{y}}_{t+h|t} = \hat{\mathbf{y}}_{t+h-1|t} + \psi_{out}(\mathbf{h}_{t+h|t}), \quad (25b)$$

for $h = 1, \dots, H$. Here, f_{init} projects the initial system state into the latent space, ϕ_{LSTM} propagates the temporal context, and ψ_{out} is a linear readout layer mapping the updated hidden state to the residual increment.

6.5 Hybrid model

The hybrid model (Physical + Residual) extends the physical predictor f_{phys} with a neural correction term that learns to compensate for unmodeled residual effects. Starting from the current measurement \mathbf{y}_t , the model recursively predicts future outputs as:

$$\begin{aligned} \hat{\mathbf{y}}_{t|t} &= \tilde{\mathbf{y}}_t, \\ \hat{\mathbf{y}}_{t+h|t} &= f_{phys}(\hat{\mathbf{y}}_{t+h-1|t}, \mathbf{u}_{t+h-1}) + \\ &\quad f_{res}(\hat{\mathbf{y}}_{t+h-1|t}, \mathbf{u}_{t+h-1}), \quad h = 1, \dots, H. \end{aligned} \quad (26)$$

where f_{phys} denotes the discrete-time physical mapping defined in (20), and f_{res} is a feed-forward neural network that outputs a residual correction $\Delta\mathbf{y}_t$ in the same representation as \mathbf{y} . The residual component is initialized to zero and progressively learns to correct systematic errors of the physical model, such as aerodynamic drag, blade interference, or motor lag.

6.6 Performance discussion

Figure 8 reports the full $MAE_{(\cdot),h}$ curves for $h = 1, \dots, 50$ across all models and averaged across the three runs of the *Melon* trajectory, while Figure 9 illustrates qualitatively the 50-step-ahead predictions on a representative segment of the first test trajectory. For clarity, Table 6 summarizes the MAE at three representative horizons ($h = 1$, $h = 10$, and $h = 50$) for the five models considered: *Naïve*, *Physics*, *Residual*, *Phys. + Res.*, and *LSTM*.

All learned models operate in a *residual* fashion: they predict state increments and construct trajectories through recursive summation, instead of predicting absolute states. Formally, each model learns:

$$\Delta \hat{y}_{t+h-1|t} = \hat{y}_{t+h|t} - \hat{y}_{t+h-1|t}, \quad (27)$$

and the multi-step prediction is obtained by accumulating these residuals. Note that any systematic bias in the learned increments compounds over time, making long-horizon prediction sensitive to model structure. Models without strong inductive priors – notably the pure neural residual model and the LSTM – are therefore more prone to drift. Indeed, feed-forward neural networks must approximate the full transition map directly from noisy data, making them especially sensitive to bias in the learned residual increments. The LSTM faces an additional limitation: its recurrent update is governed by an internal hidden state rather than explicit physical variables, making it challenging to enforce physical consistency and causing hidden-state drift to accumulate over time. In contrast, the Phys+Res model benefits from the stability of the physical integrator, requiring the network to learn only minor corrections to account for unmodelled effects. This structural prior provides a more reliable foundation for multi-step prediction, explaining its superior long-horizon performance.

For position and linear velocity, all learned models outperform the naïve integrator. The physical model and the physics-plus-residual network deliver the best performance, followed by the purely neural residual model and the LSTM. Translational dynamics are comparatively easier to identify: the mass is known with high accuracy, and the linear accelerometer provides low-noise measurements, making the thrust contribution to linear acceleration very reliable, even if torque estimation is more uncertain. This behaviour is clearly visible in the first row of Figure 9: the 50-step-ahead predictions from the learned models align closely with the *ground truth* (GT), in sharp contrast with the Naïve prediction (pink), which behaves as a pure delay. An analogous pattern is observed for the linear velocities (third row): despite the higher variability inherent to these signals, the learned models remain temporally aligned with the GT, whereas the Naïve fails to track the correct timing of the motion.

Rotational dynamics are particularly challenging to predict due to limitations in the standard quadratic motor model, which does not capture a slow, low-frequency component of the actuation dynamics and therefore introduces systematic errors in the torque prediction. The physics model mitigates this by driving the rotational motion directly from the measured angular velocity and setting its derivative to zero, preventing the instability that would arise from integrating an incorrect torque model and explaining its com-

paratively strong performance at short horizons. Learned residual models, both the feedforward and the LSTM, do not substantially improve rotational accuracy, as they are trained and evaluated on 50-step windows that are too short to resolve the underlying slow dynamics. This choice is deliberate: the benchmark targets 0.5-s multi-step prediction, and longer temporal windows would be incompatible with real-time deployment on embedded hardware such as the Crazyflie’s STM32 microcontroller. Moreover, even if trained on longer sequences, test-time rollouts would still be limited to the same short horizons, preventing reconstruction of long-timescale actuation effects. As a result, improvements in rotational prediction remain modest across baselines, pointing to the need for either more expressive temporal models with longer context or enhanced physics-based descriptions of rotor and motor dynamics.

Table 7 summarizes the main architectural and computational characteristics of the evaluated models, which we encourage practitioners to take into account when designing or assessing new benchmarks. In particular, the table lists the number of trainable parameters for each model. All learned architectures were selected to have a comparable order of magnitude in terms of parameter count, thereby avoiding biased comparisons and, most importantly, preventing excessively demanding computational loads on embedded hardware. The second column reports the number of floating-point operations (FLOPs) per forward pass. We further deploy all models in 32-bit float precision on our platform’s STM32 MCU with STM32EdgeAI Developer Cloud⁶. This service enables model benchmarking on the target MCU without having access to a Crazyflie drone, leveraging the service’s test farm of physical MCUs in the cloud. We measure the resulting inference time T^{inf} , reflecting the computational cost of running each model *on board*. Among the learned architectures, the LSTM is the most computationally demanding, with an inference time of 2.09 ms for a single one-step prediction. This is approximately twice the inference time of the purely residual feed-forward model, which is the lightest architecture.

For N -step-ahead predictions, the computational cost scales linearly as $N \times T^{\text{inf}}$. At a sampling rate of 100 Hz, this implies that only 4 to 8 steps could be predicted within a single control cycle, which may still be suitable for a short-horizon model predictive control. It is worth noting that the Physics model (and, consequently, the Phys. + Res. model) is slower than the purely residual network despite having zero trainable parameters. This is due to the more expensive operations inherent to rigid-body dynamics, such as cross products, normalization steps, and matrix–vector computations, which impose a higher computational burden on embedded hardware.

7 Conclusions

We have presented a comprehensive benchmark for nonlinear system identification on nano-quadrotors, comprising high-frequency flight data, a standardized evaluation protocol, and a suite of baseline models. Our comparative

⁶<https://stedgeai-dc.st.com>. Model export process and benchmark setup are described in our GitHub repo.

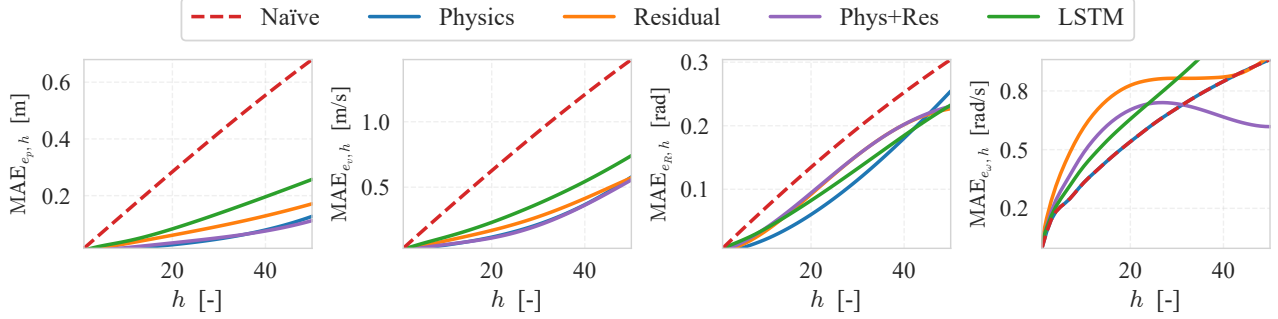


Figure 8: $\text{MAE}_{(\cdot),h}$ scores (for position, linear velocity, orientation and angular velocity) for $h = 1, \dots, 50$

Table 6: Numerical performance at $h = 1, 10, 50$. The italic column reports the cumulative simulation error (sum of MAEs over $h = 1..50$).

Model	MAE _{p,h} [m]				MAE _{v,h} [m/s]				MAE _{R,h} [rad]				MAE _{\omega,h} [rad/s]			
	<i>h=1</i>	<i>h=10</i>	<i>h=50</i>	<i>h=1:50</i>	<i>h=1</i>	<i>h=10</i>	<i>h=50</i>	<i>h=1:50</i>	<i>h=1</i>	<i>h=10</i>	<i>h=50</i>	<i>h=1:50</i>	<i>h=1</i>	<i>h=10</i>	<i>h=50</i>	<i>h=1:50</i>
Naïve	0.0143	0.1430	0.6797	17.7878	0.0329	0.3182	1.4749	38.9241	0.0071	0.0692	0.3041	8.2138	0.0796	0.3596	0.8837	29.0866
Physics	0.0013	0.0126	0.1269	2.3223	0.0080	0.0570	0.5781	10.6232	0.0011	0.0205	0.2544	5.1013	0.0796	0.3596	0.8837	29.0866
Residual	0.0032	0.0305	0.1712	<i>4.0519</i>	0.0116	0.0890	0.5720	<i>12.5809</i>	0.0022	0.0331	0.2268	6.0591	0.1138	0.5949	0.9005	35.5735
Phys+Res	0.0016	0.0166	0.1119	2.3625	0.0092	0.0613	0.5556	10.4033	0.0027	0.0376	0.2306	<i>6.1534</i>	0.0912	0.4880	0.5979	28.9873
LSTM	0.0079	0.0390	0.2572	<i>5.9711</i>	0.0247	0.1175	0.7407	<i>16.7207</i>	0.0066	0.0372	0.2325	5.6525	0.1021	0.4292	1.2407	35.8353

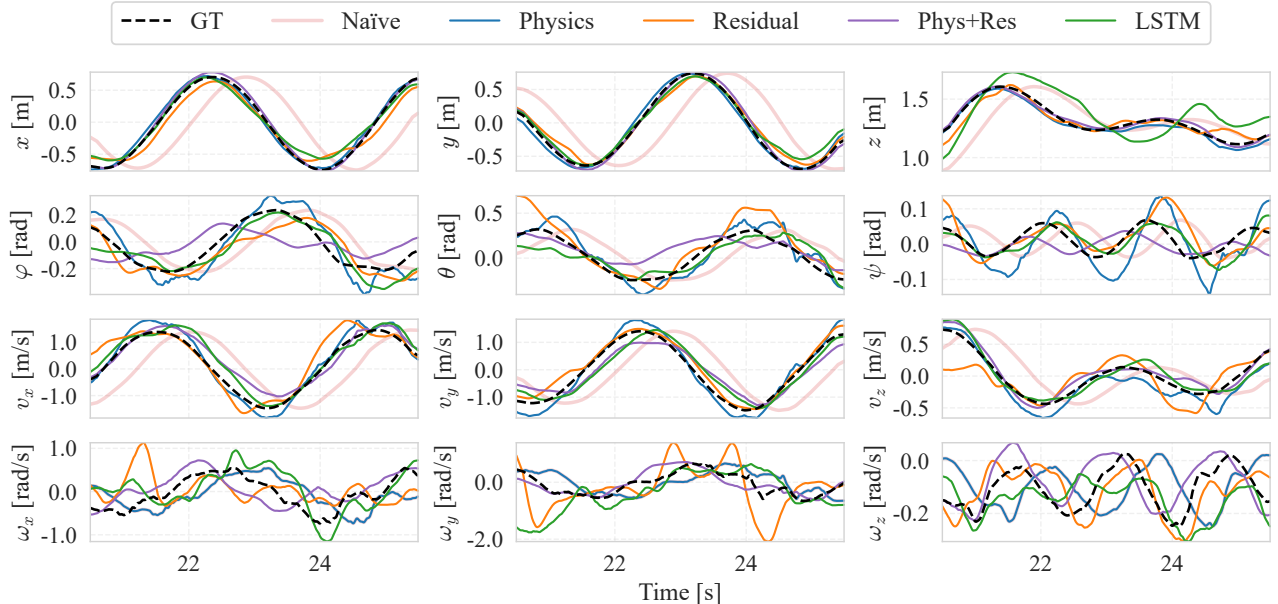


Figure 9: Output trajectories of *Melon* (run 1), from 20 to 25 s, comparing 50-step ahead predictions $\hat{y}_{t+50|t}$ from different models with respect to the ground truth y_{t+50} . Trajectories have been filtered (centered rolling mean with window 20) for visualization purpose.

analysis demonstrates that while current methods achieve high-fidelity prediction of position and linear velocity, making them viable for model-based control, accurate modeling of rotational dynamics remains a significant open challenge. A primary bottleneck is the standard quadratic motor model, which neglects low-frequency actuation dynamics that residual feedforward corrections alone cannot fully compensate. This finding suggests that future hybrid approaches must leverage temporal learning architectures or incorporate more expressive physics-based rotor models. Finally, while the proposed trajectories are sufficiently aggressive to excite non-

linearities, improved actuation modeling will likely unlock the platform’s full flight envelope. This creates a virtuous cycle where better models enable more agile data collection, further enriching the benchmark and accelerating progress in control for miniaturized aerial vehicles.

Acknowledgments

Supported by IDSIA.

Table 7: $\#\text{params}$ indicates the number of trainable parameters, Compute denotes the floating-point operations (FLOPs) per step, and T^{inf} is the average inference time measured on the target STM32 MCU.

Model	#params [k]	Compute [kFLOPs]	T^{inf} [ms]
Naïve	–	–	–
Physics	–	0.8	1.79
Residual	18.5	18.2	1.03
Phys+Res	18.5	18.2	2.82
LSTM	24.7	25.1	2.09

References

[1] Jia Deng, Wei Dong, Richard Socher, Li-Jia Li, Kai Li, and Li Fei-Fei. Imagenet: A large-scale hierarchical image database. In *2009 IEEE conference on computer vision and pattern recognition*, pages 248–255. Ieee, 2009.

[2] Marc G Bellemare, Yavar Naddaf, Joel Veness, and Michael Bowling. The arcade learning environment: An evaluation platform for general agents. *Journal of artificial intelligence research*, 47:253–279, 2013.

[3] Zhenqin Wu, Bharath Ramsundar, Evan N Feinberg, Joseph Gomes, Caleb Geniesse, Aneesh S Pappu, Karl Leswing, and Vijay Pande. Moleculenet: a benchmark for molecular machine learning. *Chemical science*, 9(2):513–530, 2018.

[4] Max Champneys, Gerben I Beintema, Roland Tóth, Maarten Schoukens, and Timothy J Rogers. Baseline results for selected nonlinear system identification benchmarks. *IFAC-PapersOnLine*, 58(15):474–479, 2024.

[5] Maarten Schoukens and Jean Philippe Noël. Three benchmarks addressing open challenges in nonlinear system identification. *IFAC-PapersOnLine*, 50(1):446–451, 2017.

[6] Ravindu G Thalagala, Oscar De Silva, Awantha Jayasiri, Arthur Gubbels, George KI Mann, and Raymond G Gosine. Mun-frl: a visual-inertial-lidar dataset for aerial autonomous navigation and mapping. *The International Journal of Robotics Research*, 43(12):1853–1866, 2024.

[7] Jeffrey Delmerico, Titus Cieslewski, Henri Rebecq, Matthias Faessler, and Davide Scaramuzza. Are we ready for autonomous drone racing? the UZH-FPV drone racing dataset. In *2019 International Conference on Robotics and Automation (ICRA)*, pages 6713–6719. IEEE, 2019.

[8] Michael Burri, Janosch Nikolic, Pascal Gohl, Thomas Schneider, Joern Rehder, Sammy Omari, Markus W Achtelik, and Roland Siegwart. The euroc micro aerial vehicle datasets. *The International Journal of Robotics Research*, 35(10):1157–1163, 2016.

[9] Leonard Bauersfeld, Elia Kaufmann, Philipp Foehn, Sihao Sun, and Davide Scaramuzza. Neurobem: Hybrid aerodynamic quadrotor model. *arXiv preprint arXiv:2106.08015*, 2021.

[10] Lorenzo Lamberti, Elia Cereda, Gabriele Abbate, Lorenzo Bellone, Victor Javier Kartsch Morinigo, Michał Barciś, Agata Barciś, Alessandro Giusti, Francesco Conti, and Daniele Palossi. A sim-to-real deep learning-based framework for autonomous nano-drone racing. *IEEE Robotics and Automation Letters*, 9(2):1899–1906, 2024. doi: 10.1109/LRA.2024.3349814.

[11] S Bonato, SC Lambertenghi, E Cereda, A Giusti, and D Palossi. Ultra-low power deep learning-based monocular relative localization onboard nano-quadrotors. In *2023 IEEE International Conference on Robotics and Automation (ICRA)*, pages 3411–3417. IEEE, 2023.

[12] M Szécsi, B Györök, Á Weinhardt-Kovács, GI Beintema, M Schoukens, T Péni, and R Tóth. Deep learning of vehicle dynamics. *IFAC-PapersOnLine*, 58(15):283–288, 2024.

[13] Babak Akbari, Justin Frank, and Melissa Greeff. Tiny learning-based MPC for multirotors: Solver-aware learning for efficient embedded predictive control. *arXiv preprint arXiv:2410.23634*, 2024.

[14] Elia Cereda, Alessandro Giusti, and Daniele Palossi. Training on the fly: On-device self-supervised learning aboard nano-drones within 20 mw. *IEEE Transactions on Computer-Aided Design of Integrated Circuits and Systems*, 43(11):3685–3695, 2024. doi: 10.1109/TCAD.2024.3447208.

[15] Robert J. Wood, Benjamin Finio, Michael Karpelson, Kevin Ma, Néstor O. Pérez-Arcanibia, Pratheeve S. Sreetharan, Hiro Tanaka, and John P. Whitney. Progress on “Pico” air vehicles. In Henrik I. Christensen and Oussama Khatib, editors, *Robotics Research : The 15th International Symposium ISRR*, pages 3–19. Springer International Publishing, Cham, 2017. ISBN 978-3-319-29363-9. doi: 10.1007/978-3-319-29363-9-9.

[16] Vlad Niculescu, Daniele Palossi, Michele Magno, and Luca Benini. Fly, wake-up, find: Uav-based energy-efficient localization for distributed sensor nodes. *Sustainable Computing: Informatics and Systems*, 34:100666, 2022.

[17] Sihao Sun, Coen C de Visser, and Qiping Chu. Quadrotor gray-box model identification from high-speed flight data. *Journal of Aircraft*, 56(2):645–661, 2019.

[18] Mohamed AA Ismail, Mohssen E Elshaar, Ayman Abdallah, and Quan Quan. Dronepropa: Motion trajectories dataset for defective drones. *Data in Brief*, page 111589, 2025.

[19] Julian Förster. System identification of the crazyflie 2.0 nano quadrocopter. B.S. thesis, ETH Zurich, 2015.

- [20] Fadri Furrer, Michael Burri, Markus Achtelik, and Roland Siegwart. RotorS—a modular gazebo MAV simulator framework. In *Robot Operating System (ROS) The Complete Reference (Volume 1)*, pages 595–625. Springer, 2016.
- [21] Wojciech Giernacki, Mateusz Skwierczyński, Wojciech Witwicki, Paweł Wroński, and Piotr Kozierski. Crazyflie 2.0 quadrotor as a platform for research and education in robotics and control engineering. In *2017 22nd international conference on methods and models in automation and robotics (MMAR)*, pages 37–42. IEEE, 2017.
- [22] Robert Mahony, Vijay Kumar, and Peter Corke. Multirotor aerial vehicles: Modeling, estimation, and control of quadrotor. *IEEE robotics & automation magazine*, 19(3):20–32, 2012.
- [23] Daniel Mellinger and Vijay Kumar. Minimum snap trajectory generation and control for quadrotors. In *2011 IEEE international conference on robotics and automation*, pages 2520–2525. IEEE, 2011.
- [24] Mark W. Mueller, Michael Hamer, and Raffaello D’Andrea. Fusing ultra-wideband range measurements with accelerometers and rate gyroscopes for quadrocopter state estimation. In *2015 IEEE International Conference on Robotics and Automation (ICRA)*, pages 1730–1736, 2015. doi: 10.1109/ICRA.2015.7139421.
- [25] Mark W. Mueller, Markus Hehn, and Raffaello D’Andrea. Covariance correction step for kalman filtering with an attitude. *Journal of Guidance, Control, and Dynamics*, 40(9):2301–2306, 2017.
- [26] Du Q Huynh. Metrics for 3d rotations: Comparison and analysis. *Journal of Mathematical Imaging and Vision*, 35(2):155–164, 2009.
- [27] Joan Solà, Jeremie Deray, and Dinesh Atchuthan. A micro lie theory for state estimation in robotics, 2021. URL <https://arxiv.org/abs/1812.01537>.